UC Irvine
UC Irvine Previously Published Works

Title
Corrosion of 316 SS in direct contact with Zircaloy-4 in repository relevant conditions

Permalink
https://escholarship.org/uc/item/0r34q9hw

Journal
Journal of Nuclear Materials, 627

ISSN
0022-3115

Authors
Nguyen, Steven
Weber, Juliane
Zhang, Maximilian
et al.

Publication Date
2026-05-01

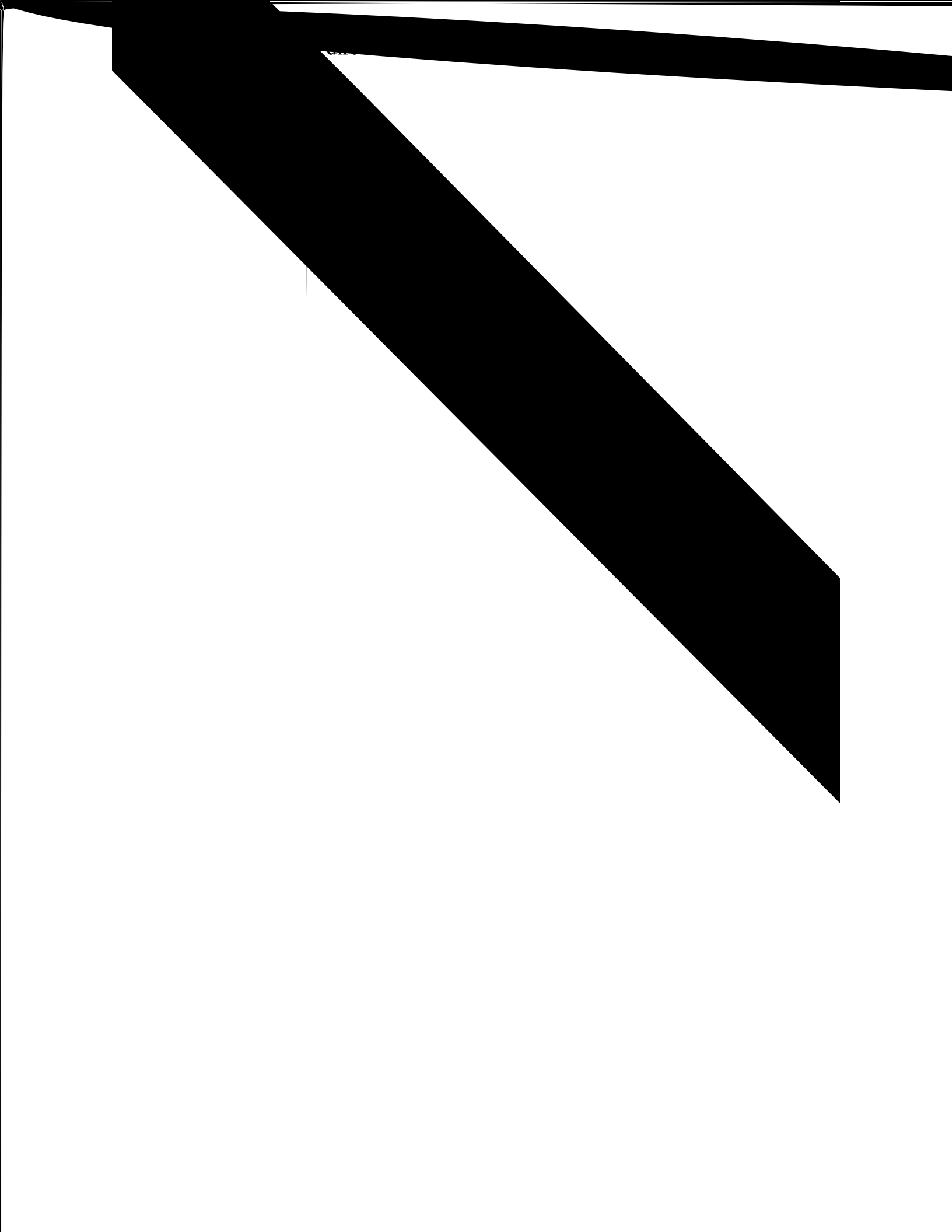
DOI
10.1016/j.jnucmat.2026.156516

Supplemental Material
https://escholarship.org/uc/item/0r34q9hw#supplemental

Copyright Information
This work is made available under the terms of a Creative Commons Attribution License, available at https://creativecommons.org/licenses/by/4.0/

Peer reviewed

eScholarship.org Powered by the California Digital Library
University of California



1. Introduction

Commercial nuclear power plants for energy conversion methods mainly utilize UO_2 as fuel [1]. The conventional cladding material consists of Zircaloy-4 and deep geological repository concepts in the United States are considering 316 stainless steel (316 SS) as the inner canister material for the final disposal concept in the proposed dual-purpose canister concept [2,3]. While there is consensus on the disposal of spent nuclear fuel (SNF) in a deep geological repository (DGR), questions on the safety case assessment remain on how the corrosion and degradation mechanisms of one engineered barrier material may affect the performance of other nearby materials. Our study therefore aims to address open questions regarding how the redox potential evolves due to corrosion scenarios in case of water intrusion into a DGR. The current study focuses on corrosion of stainless steel and Zircaloy-4 in MilliQ water as benchmarking system as well as in synthetic Mont Terri water to mimic conditions in a generic DGR in argillite host rock. An in-depth understanding of corrosion mechanisms of Zircaloy-4 and 316 SS in direct contact, which may be possible during disposal of SNF in a DGR, will help inform future studies for more complex systems that involve SNF. Deriving a fundamental understanding about the redox pairs of the fuel cladding and waste canister material evolving under water intrusion conditions is needed to decipher their influence towards the mobility of uranium in case of water intrusion into a DGR, thus answering open questions of the matrix corrosion of SNF. This study addresses questions for the later stages of the DGR safety case assessment, since it would require breaching of the waste canister as well as the cladding material. Previous single component corrosion studies showed that 316 SS experiences limited surface corrosion in the low oxygen environments expected in a repository [4–6]. As for Zircaloy-4, it has been shown to consistently form a passivating zirconium oxide layer in the form of baddeleyite (m-ZrO_2) that protects the cladding surface [7,8]. However, there is a knowledge gap on the effect of direct contact of the technical barriers in a DGR towards evolving redox conditions. When two metals are in direct contact, the fluid in between them can become confined. From physical chemistry research it is known that confinement will change the properties of confined fluids [9–13]. Therefore, it can be expected that the extrapolation of single component corrosion experiments towards multi-component systems is an oversimplification. Past studies have reported that stainless steel corrosion in the absence of UO_2 and in presence of bentonite backfill material stimulates mineral growth at the bentonite-canister interface and destabilizes trace pyrite in bentonite [14], which may have implications towards how the redox chemistry of a repository will develop over its long lifespan.

Our study focuses on the direct contact corrosion of 316 SS and Zircaloy-4 in MilliQ water and synthetic Mont Terri water. The MilliQ water serves as a benchmarking solution for our corrosion studies, whereas Mont Terri water is one of the reference corrosion media for DGR studies and mimics the composition of the Opalinus Clay water in the Mont Terri Rock Laboratory [15], which is the host to Opalinus Clay formation in Switzerland. 316 SS and Zircaloy-4 will be hydrothermally corroded at elevated temperatures to accelerate corrosion for analysis in a reasonable time span.

The experimental setup of direct contact of 316 SS and Zircaloy-4 aim to consider confinement effects which have been shown to change the properties of the interfacial water layer [9–13]. To analyze corrosion products, we combined SEM (Scanning Electron Microscopy), Raman spectroscopy, and GI-XRD (Grazing Incidence X-Ray Diffraction). Solution pH was monitored and cation concentration was measured using Inductively coupled plasma-mass spectrometry (ICP-MS). This study provides new experimental insights into the corrosion behavior of the two component 316 SS/Zircaloy system, which is crucial for understanding the multi-component system of spent nuclear fuel in contact with cladding and waste canister materials in a DGR.

2. Materials & methods

2.1. Sample and synthetic Mont Terri Water preparation

Thin sheets (< 2 mm) of 316 SS and Zircaloy-4 (McMaster-Carr, American Elements) were cut to create coupons measuring 3 cm x 1.5 cm and were then wet-polished with deionized water by hand using 600-grit and 1200-grit silicon carbide papers followed by rinsing with deionized water and acetone (VWR International, ≥ 99.5 %). No additional heat treatment was performed on either the 316 SS or Zircaloy-4 coupons. Fig. 1 shows the resulting surface after polishing while SI Table S1 and S2 show the compositions of 316 SS and Zircaloy-4 from the vendors. GI-XRD analysis of the polished coupons are shown in SI Figure S1 and S2.

The clean coupons were then stored in a desiccator containing drierite and were weighted prior to corrosion experiments. The sandwiched coupons were prepared by securely fastening 316 SS and Zircaloy-4 together using platinum. A schematic of the sandwiched experiments detailing the metal-metal and metal-water interface is given in SI Figure S3.

Synthetic Mont Terri Water was prepared by mimicking the chemical composition of the groundwater observed at the Mont Terri site [16]. NaCl (VWR Life Science, ≥ 99.9 %), KCl (Fisher Chemical, 99 %), $MgCl_2{\cdot}6H_2O$ (Honeywell, ≥ 99 %), $NaHCO_3$ (Fisher Chemical, 99.7 %), and $CaSO_4{\cdot}2H_2O$ (Sigma-Aldrich, ≥ 99 %) were used as received to obtain the desired chemical composition. The targeted composition of the synthetic Mont Terri water is described in Table 1, being based on information provided in the open literature [15,16]. These salts were dissolved in deionized water (18.2 MΩ-cm) to prepare the synthetic Mont Terri water. The synthetic Mont Terri water was then stirred with a stir bar at room temperature overnight and its pH was measured with an Orion 4-Star pH meter and a Fisherbrand accumet pH probe. The pH meter was calibrated using pH buffer solutions (Potassium Biphthalate, 4.00 ± 0.02 @ 25 °C, Dibasic Sodium Phosphate and Monobasic Potassium Phosphate, 7.00 ± 0.02 @ 25 °C, Sodium Carbonate and Sodium Bicarbonate, 10.00 ± 0.02 @ 25 °C). All pH measurements were taken at room temperature.

2.2. Hydrothermal corrosion experiments

Hydrothermal corrosion experiments were conducted with corrosion durations from 1 to 6 weeks, having both temperature (150 °C and 250 °C) and the corrosion medium (MilliQ water 18.2 MΩcm) and simulated Mont Terri water) as additional parameters to observe their influence towards the corrosion between 316 stainless steel (316 SS) and Zircaloy-4.

Prior to hydrothermal corrosion in sandwiched coupon experiments, the selected water type was degassed by sparging with Argon gas (99.99 % purity) for 1 hour. The pH measurements on the degassed solution were performed and, in the case of experiments using Mont Terri water, the pH was adjusted to roughly 7.5 using HCl (MilliporeSigma, 3 M Reagent Grade) to match the anticipated near-neutral pH of the ground water [15,17,18]. Wired coupons along with 15 mL of the degassed solution were then placed in their own 45 mL Parr 4744 PTFE-lined digestion vessel autoclave [19]. The autoclave was then sealed and placed in a SHEL LAB oven at the desired temperature and duration for hydrothermal corrosion. Approximately 30 mL of air remained in the PTFE liner, which may have generated initial oxidizing conditions that promote hematite formation.

After termination of the experiment, the autoclaves were allowed to cool down ambiently to room temperature for 1–2 hours. The corroded coupons were removed from the corrosion solution and gently rinsed with deionized water before being stored in a desiccator for future analysis. The pH of the remaining corrosion solution was measured after reaching room temperature. Precipitates in the corrosion solution were separated by centrifuging at 4400 rpm for 5 minutes and collected for XRD analysis. Prior to secondary phase analysis, the sandwiched

coupons were disassembled. 1 mL of 70 % HNO_3 (Honeywell, 70 % Reagent Grade) was added to 10 mL of the corrosion solution to stabilize the corrosion solution for later ICP-MS analysis, and a 100-fold dilution sample was prepared for each corrosion experiment using a solution of 1 % ultra-high purity HNO_3.

2.3. Analytical techniques

ICP-MS analysis was performed using the Thermo Scientific™ iCAP™ RQ single quadrupole (SQ) ICP-MS provided at UCI's Irvine Materials Research Institute (IMRI) facility. All samples were measured in the standard measurement mode with a dwell time of 0.1 seconds. Prior to sample analysis the instrument was calibrated with ICP mix standards (ICP Mix Standard 5, Inorganic Ventures, 5 % v/v Nitric Acid and ICP Mix Standard 3, Inorganic Ventures, 5 % v/v Nitric Acid /tr hydrofluoric acid) prepared to detect iron, nickel, chromium, and zirconium ions in solution after corrosion. Details on detection limits and signal to noise is given in the supporting information (Table S3 and Table S4).

Secondary electron and backscattered electron images were taken with a TESCAN Mira 3 SEM instrument at 20 kV. For starting material characterization, SEM characterization was performed at 8 kV. Corroded samples were taken as is from the desiccator for SEM analysis. Elemental analysis was performed using Energy-dispersive X-ray spectroscopy (EDS) with a EDAX Octane Elite detector.

Raman spectra were collected using a Raman microscopy system based on a Renishaw InVia microscope with a 2400 gr/mm grating at the Laser Spectroscopy Laboratories at UCI. Samples were probed with a 532 nm laser at a lowered power ranging from 0.3 - 3 mW. The produced spectra were normalized to the highest intensity band with the background being subtracted and cosmic rays removed.

X-ray diffraction data of precipitates were collected using a Proto AXRD benchtop diffractometer, with Cu Kα radiation (λ=0.154 nm, 40 kV, 40 mA). Grazing incidence diffraction data was collected using the Rigaku Smartlab X-ray Diffractometer at UCI's IMRI facility, which also uses Cu Kα radiation. The angle of incidence was set between 0.3 and 0.4 for surface analysis of corroded coupons.

2.4. Thermodynamic modeling

Speciation calculations at equilibrium and its corresponding pH were performed with HCh code version 4.4 at 150 °C and 250 °C, both at the saturated pressure using the free energy minimization algorithm and the Unitherm database [20]. A 13-component system of H-O-Fe-Cr-Ni-Zr-C-Ca-Cl-K-Mg-Na-S was modeled to replicate a system representing the major elements of the 316 SS waste canister (Fe, Cr, Ni) and Zircaloy-4 cladding (Zr) interacting with synthetic Mont Terri water. From this system, a total of 53 possible individual phases and 63 possible aqueous phases in solution were selected using thermodynamic values provided by Holland [21], Stoffregen [22], Robie [23], Naumov [24], IVTANTERMO [25], Glushko [26], Lemire [27], Johnson [28], Shock [29], Sverjensky [30], Tagirov [31], and Diakonov [32]. A detailed list of the considered phases and species for thermodynamic modeling are provided in (SI Table S5 and S6). The amount of water and species present in the experimental corrosion experiments were scaled up to 1 kg of water. Species that require sulfate reduction have been excluded from the modeling system due to sulfate reduction being known to be kinetically hindered [33]. Hypochlorite species were also excluded from the modeling system since they would be too oxidizing to form in the generally reducing environment observed in the Mont Terri site [34]. Redox potential calculations between solid phases were performed using the Unitherm software in the HCh package.

Table 1
Targeted composition of the synthetic Mont Terri groundwater made to mimic the approximated parameters of the groundwater from the Mont Terri site [15,16].

Species	Concentration [mg/L] Target Composition
Ca^{2+}	421
K^{+}	221
Mg^{2+}	182
Na^{+}	3885
Cl^{-}	5672
SO_4^{2-}	2305
CO_3^{2-}	162
pH	7.50

3. Results and discussion

3.1. Corrosion in MilliQ water – experiments at 150 °C

During the corrosion of 316 SS/Zircaloy-4 sandwiches in MilliQ water, both precipitates in solution are formed as well as secondary phases on the two metals (Fig. 2). Precipitates in solution were observed as early as 1 week into corrosion and persist throughout weeks 1–6. XRD

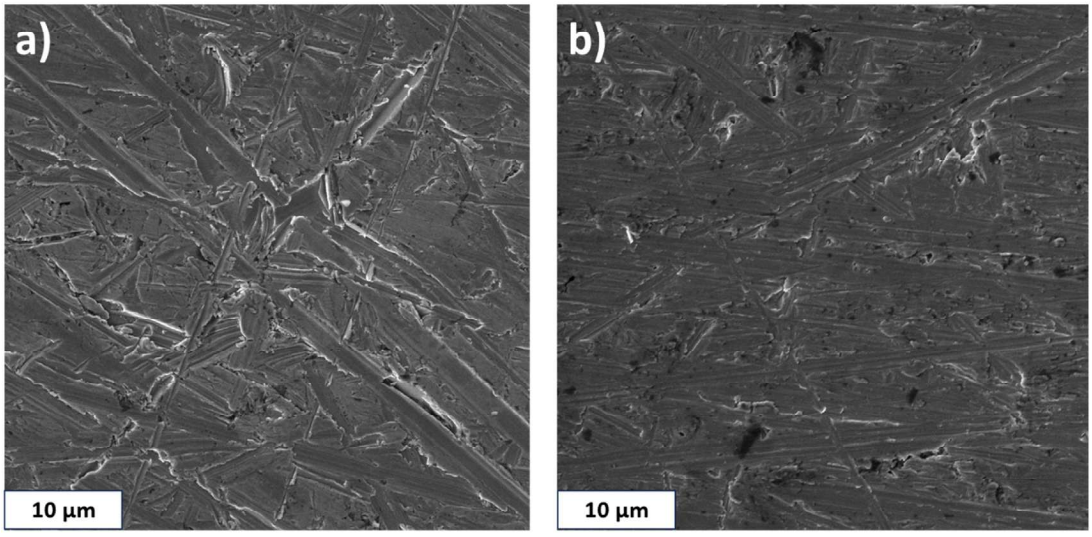


Fig. 1. SEM-SE images of the surface of 316 SS (a) and Zircaloy-4 (b) after wet-polishing with silicon carbide papers.

shows that the precipitates consist of hematite (α-Fe_2O_3) (Fig. 2a). Results may be affected by the acidification procedure due to magnetite (Fe_3O_4) being more soluble [35] at lower pH environments, leading to preferential dissolution of magnetite.

Micrometer-sized iron oxides (1–10 μm) confirmed by EDS analysis form on the peripheries of both Zircaloy-4 and 316 SS at all interfaces (Figure 2b+*c*). Iron oxides were more commonly observed on the metal-to-metal interface and increase in quantity with increasing corrosion durations. Iron oxides exhibit granular and plate-like morphologies (Figure 2b+*c*). Raman spectroscopy was used to identify the iron oxides as hematite and magnetite (Fig. 2d). For magnetite, only the characteristic A_{1g} band at 663 cm^{-1} was observed [36–38] which may indicate its existence as a minor iron oxide phase. For hematite, two of its A_{1g} modes are observed at 231 cm^{-1} and 503 cm^{-1} alongside all of its predicted E_g modes at 241 cm^{-1}, 299 cm^{-1}, and 615 cm^{-1} [37,38]. The intense magnon mode of hematite at ~1300 cm^{-1} is also observed [39, 40]. As corrosion duration increases, hematite remains as the dominant iron oxide whereas magnetite remains as a minor phase. The consistent identification of hematite suggests that chemical environment in MilliQ water at 150 °C favors hematite formation.

Maghemite (γ-Fe_2O_3), a possible intermediate during the oxidation of magnetite into hematite [41,42], was not observed by Raman spectroscopy and can thus provide information on how hematite develops in this system [43,44]. The absence of a maghemite intermediate suggests that the dominant route for hematite formation is not by the direct oxidation of initially formed magnetite. Instead, the hematite precipitates forming in solution is likely caused by the direct oxidation of aqueous Fe^{2+} in solution [45] that is assisted by the residual oxygen present in the headspace of the PTFE liner. As for the hematite identified on the 316 SS and Zircaloy-4 surface, it may be forming through a non-redox acid-base reaction where magnetite transforms into hematite as described in Eq. (1) [45–47].

$$Fe_3O_4 \text{ (magnetite)} + 2H^+ \leftrightarrow Fe_2O_3 \text{ (hematite)} + Fe^{2+} + H_2O \quad (1)$$

GI-XRD was able to detect baddeleyite (m-ZrO_2) and tetragonal zirconia (t-ZrO_2) as early as 1 week of corrosion at the metal-to-water interface of the Zircaloy-4 at an incident angle of 0.4° (Fig. 2e). XRD reflexes pertaining to the bulk uncorroded zirconium in Zircaloy-4 remain prominent, suggesting that the Zircaloy-4 coupon may be passivated by the ZrO_2 layer. No secondary phases originating from the oxidation of the Zircaloy-4 coupon could be observed by Raman spectroscopy. Although, this may be due to the ZrO_2 being thin enough such that Raman spectroscopy is unable to detect it.

Fig. 3a shows that the pH of the corrosion solution from MilliQ water experiments remains below the neutral pH of 7 as corrosion proceeds. The corrosion solution reaches its maximum pH value of 6.7 ± 0.2 after 1 week of corrosion before decreasing to a pH of 5.5 ± 0.6 after 6 weeks of corrosion. Solution analysis via ICP-MS shows Fe to be the most abundant species, followed by Ni, Cr, and Zr. Fe and Cr both follow a similar trend where their concentration increases before stabilizing to a lower concentration whereas the concentration of zirconium remains low and unchanged throughout the entire duration of the corrosion experiments. The iron concentration fluctuates between 50–160 ppm during the 1–6 week corrosion period. Iron concentration maximizes at ~160 ppm after 2 weeks of corrosion and decreases to ~116 ppm after 6 weeks of corrosion. Zr concentration is on average 0.1 ppm, with maximum concentration of 0.2 ppm 6 weeks into corrosion and minimum being 0.1 ppm 3 weeks into corrosion as shown in SI Figure S4. Nickel concentrations were also measured due to these elements being another major component of 316 SS; ICP-MS results show that nickel concentrations increase to a maximum concentration of 39 ppm after two weeks into corrosion before stabilizing to a lower concentration of ~34 ppm as described in SI Figure S4.

Based on solid phase analysis showing mainly iron oxides and the

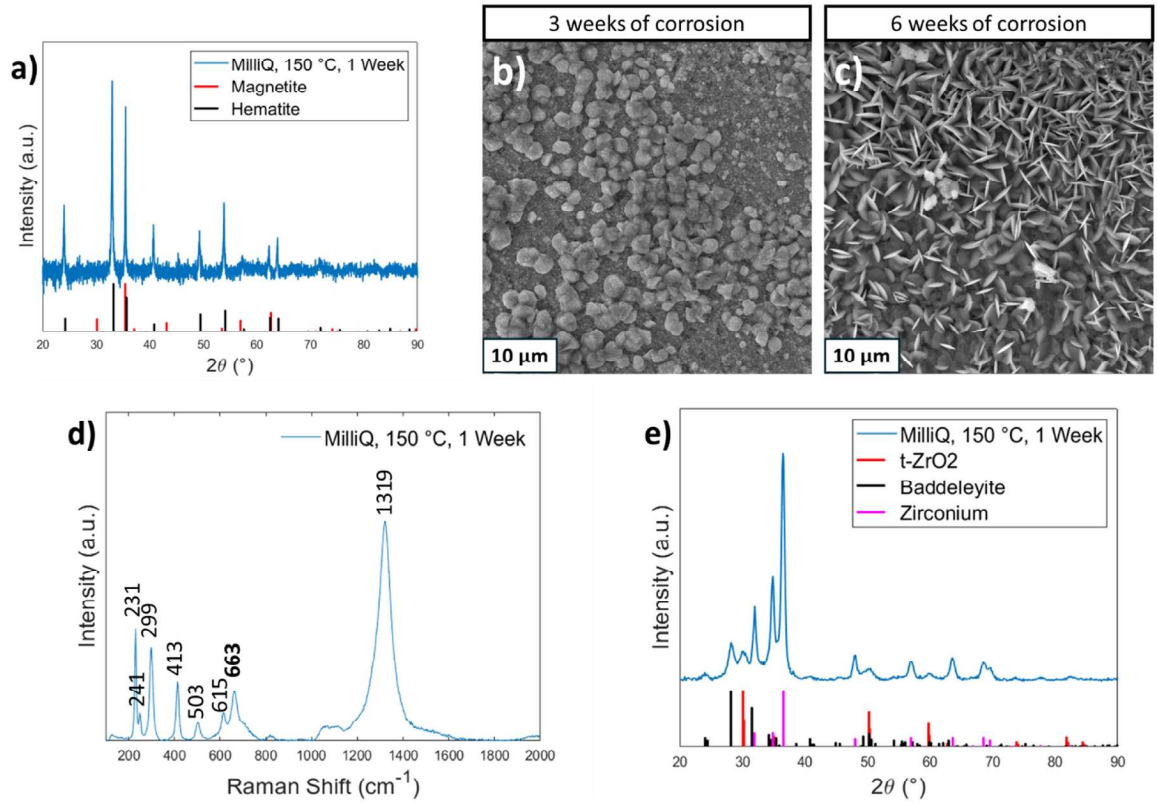


Fig. 2. Solid characterization after corrosion in MilliQ water at 150 °C. a) XRD of precipitates from MilliQ water after 1 week. SEM-SE images of newly formed iron oxides at the metal-to-metal interface of 316 SS after b) 3 weeks and c) 6 weeks. d) Raman analysis of 316 SS metal-to-metal interface after 1 week. Labeled bands belong to hematite (α-Fe_2O_3) and to magnetite (bold). e) GI-XRD of Zircaloy-4 surface at the metal-to-water interface after 1 week.

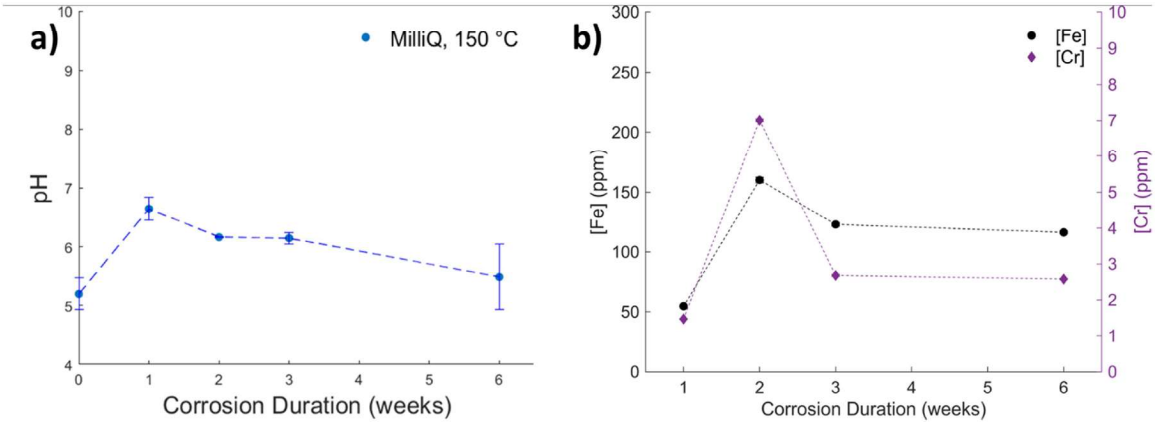


Fig. 3. Aqueous analysis for corrosion experiments at 150 °C in MilliQ water. a) pH development. b) Concentration as a function of time as measured by ICP-MS for iron and chromium. The error bars in (b) are covered by the data points in the plot. Detection limits for Fe is 0.5 ppb and for Cr is 11 ppt.

high concentration of iron in solution compared to the other major elements in 316 SS and Zircaloy-4, it can be assumed that iron-based reactions are the main driving force in the MilliQ water system at 150 °C. pH and ICP-MS analysis agree with our hypothesis that the non-redox acid-base reaction described in Eq. (1) is controlling hematite formation after the initial oxidation of iron from 316 SS. The mildly acidic pH would supply the MilliQ solution with the protons needed to have magnetite transform into hematite, releasing Fe^{2+} into solution that can then be oxidized into the hematite precipitates observed after 1 week of corrosion. This observation can be seen in the liquid phase results, where the observed increase in pH after 1 week coincides with the point where iron concentration is the lowest. This would indicate consumption of protons to have magnetite transform into hematite and release Fe^{2+}, followed by the oxidation of released Fe^{2+} to generate hematite precipitates in solution. The later behavior in pH and iron concentration after 1 week may be attributed to continued transformation of magnetite into hematite described in Eq. (1). Depletion of the residual oxygen may lead to the observed increase in iron concentration to keep released Fe^{2+} in solution. The following stabilization of both pH and concentration may be explained by Eq. (1) also acting as a buffer for both pH and iron concentrations [47], since it is also a reversible reaction.

In summary, during corrosion in MilliQ water, hematite (α-Fe_2O_3) and magnetite (Fe_3O_4) form as secondary phases originating from 316 SS whereas baddeleyite monoclinic zirconia (m-ZrO_2) and tetragonal zirconia (t-ZrO_2) form as secondary phases (Fig. 2) originating from the Zircaloy-4. Results suggest that MilliQ water experiments in 150 °C are dominated by iron chemistry that is controlled by a mixture of both redox dependent and redox independent reactions. The lack of a maghemite intermediate despite traces of magnetite being detected alongside hematite suggests that redox independent mechanisms probably occurred on the metal surfaces where magnetite is present. Redox dependent reactions, namely the oxidation of Fe^{2+} into Fe^{3+}, might occur more often in solution to generate hematite precipitates. Iron oxides develop on both 316 SS and Zircaloy-4 at both metal-water and metal-metal interfaces, but were more common at the metal-metal interface. This may be a result of increased chemical interaction at the solid/liquid interface due to modified interfacial water structure, which is known to be different than bulk solution [48] as reported in other hydrothermal corrosion studies involving stainless steel [49].

3.2. *Corrosion in MilliQ water – experiments at 250 °C*

Micrometer-sized iron oxides (most ~1–10 μm with some larger crystals of 10 μm-15 μm) consistently form on the peripheries of both Zircaloy-4 and 316 SS at the metal-to-metal interface. At 250 °C octahedrons were observed (Fig. 4a), which was not observed in MilliQ experiments at 150 °C. Compared to observations in MilliQ experiments at 150 °C, iron oxides become more prominent at the metal-to-metal interface of both 316 SS and Zircaloy-4 rather than at the metal-to-water interface. Hematite remains as an iron oxide at the elevated temperature scenario (SI Figure S5), although magnetite appears to be more common, based on Raman analysis detecting magnetite with its additional supporting T_{2g} bands (186 cm^{-1}, 480 cm^{-1}, 547 cm^{-1}) and E_g band (318 cm^{-1}) (Fig. 4b) [35,36] as early as 1 week into corrosion on both metals at the metal-to-metal interface. Pure magnetite was detected more frequently than hematite when compared to MilliQ water experiments conducted at lower temperatures as shown in Fig. 4c, where no Raman bands of hematite were observed. This observation of magnetite being more present through Raman spectroscopy coincides with the appearance of octahedral iron oxides also seen by the Raman microscope (SI Figure S6), which are often attributed to the formation of magnetite [50–52] and therefore seems to imply that elevated temperatures enhances the development of magnetite. Very rarely, in localized areas of the coupon at the metal-to-metal interface, octahedral iron oxides can be observed with holes in them (Fig. 4c). The development of holes on the iron oxides suggests localized corrosion that is analogous to pitting corrosion [53], or perhaps localized dissolution of the iron oxides. Based on the assumption that the octahedral iron oxides represent magnetite, the formation of the holes may be caused by the increased auto--ionization of water at higher temperatures providing localized areas of low pH that will assist in magnetite dissolution [35]. Because the developed iron oxides lack the chromium and nickel that make the bulk 316 SS coupon corrosion resistant [53], it could be the cause for why the development of holes is only observed on the iron oxides, and not on the surface of 316 SS. Nonetheless, this observation suggests that while magnetite formation is promoted at higher temperatures, it is sensitive to localized changes in the chemical environment and likely won't act as a passivating oxide for 316SS. Alternatively, the development of holes on the octahedral crystals may be due to hopper crystal growth wherein the edges of the crystal develop more quickly than the faces [54], potentially leading to an appearance that is similar to that of a hole on the crystal structure.

No new secondary phases were observed from Zircaloy-4 at the elevated corrosion temperature of 250 °C, although baddeleyite is now able to be detected as early as 1 week into corrosion at both interfaces of Zircaloy-4 by Raman spectroscopy as indicated by the A_{1g} modes at 175 cm^{-1}, 474 cm^{-1}, 555 cm^{-1}, 636 cm^{-1}, and the two B_g modes at 333 cm^{-1} and 380 cm^{-1} [55,56] (Fig. 4d). Zirconia is also visible in SEM-BSE images and EDS maps (SI Figure S7). Tetragonal zirconia remains undetected by Raman, and no change is observed in the Raman stretches of monoclinic zirconia as corrosion duration increases. Results therefore suggest that temperature accelerates growth of specifically baddeleyite while providing a negligible influence on tetragonal phase ZrO_2.

Nanometer sized plate-shaped secondary phases not observed in 150

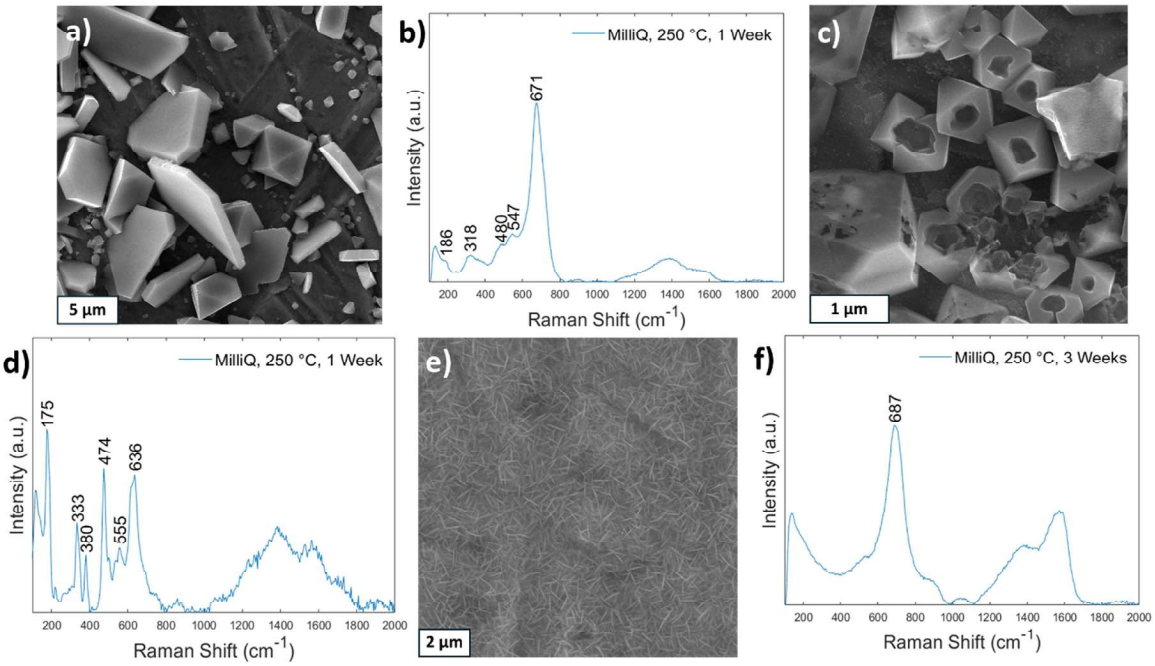


Fig. 4. Solid characterization after corrosion in MilliQ water at 250 °C. a) SEM-SE image of 316 SS metal-to-metal interface showing iron oxides of different morphologies (platelets and octahedrons). Raman spectroscopy is now able to detect b) magnetite after 1 week on the metal-to-metal interface of 316 SS. c) Some iron oxides contain holes. d) Raman spectroscopy of m-ZrO_2 at the metal-to-water interface of Zircaloy-4 for 1 week. e) SEM-SE image of the nanometer-sized chromium-rich plates. f) Raman spectra identifying the chromium phase as chromite at the metal-metal interface of 316 SS after 3 weeks.

°C MilliQ experiments formed only at the metal-to-metal interface on the 316 SS surface as early as 1 week of corrosion. The plate-shaped secondary phases are located closer to the center face of the 316 SS, away from the iron oxides that preferentially form near the coupon edges (Fig. 4e). Additionally, these phases often formed on cracks at the metal-to-metal interface of 316 SS (SI Figure S8). EDS analysis shows that the nanometer phases contain higher chromium than iron content which implies formation of a chromium-rich nanometer-sized phase. GI-XRD analysis of this phase identified it as chromite ($FeCr_2O_4$) (SI Figure S9). Raman analysis confirms the identification as chromite due to the presence of the strong characteristic Raman band at ~690 cm^{-1} caused by the A_{1g} Cr-O vibration from the CrO_6 octahedral unit of chromite [57–60] (Fig. 4f). While magnetite and chromite do share the same XRD pattern due to their spinel crystal structure, the larger chromium content observed by EDS and the lack of Raman bands pertaining to magnetite strongly suggest that these nanometer phases are chromite and not magnetite.

No visible precipitates from solution were observed until 3 weeks of corrosion. This differs from experiments performed at 150 °C, where precipitates can be observed after 1 week. The amount of precipitates after 3 weeks of corrosion at 250 °C was too small for any identification analysis. XRD analysis on precipitates formed after 6 weeks showed hematite reflexes and some low-intensity reflexes that correspond to magnetite (SI Figure S10).

Similar to the 150 °C corrosion experiments in MilliQ water, the pH remains consistently below the neutral pH of 7 but reaches a slightly more acidic pH (pH = 5.201 equivalent to an increase of 5.7 %) compared to the 150 °C MilliQ experiments after 6 weeks of corrosion. The pH steadily decreases to 4.3 ± 0.3 after three weeks of corrosion before rising to 5.2 ± 0.1 at 6 weeks. Solution analysis via ICP-MS shows again Fe to be the most abundant species in solution, followed by Ni, Cr, and Zr. An overview of all measured concentrations is given in (SI Table S7). The iron concentration ranges from 10 — 128 ppm between the 1–6 week corrosion duration (Fig. 5). Similar to the ICP-MS results at 150 °C in MilliQ water (Fig. 3b), iron and chromium show a similar trend of increasing concentration with corrosion experiment duration (Fig. 5). Although, unlike the results in the 150 °C MilliQ experiments, the iron concentration remains relatively low until 6 weeks of corrosion. The behavior of zirconium is near identical as at 150 °C, with overall concentration being below 0.2 ppm.

Based on previous discussion in the 150 °C MilliQ experiments, the acidic environment of the MilliQ solution should promote hematite formation by Eq. (1). However, pure octahedral magnetite is commonly detected in just 1 week of corrosion which would imply the suppression of the forward reaction of Eq. (1). This may be due to interactions at elevated temperatures and the increased auto-ionization of water shifting Eq. (1) to favor magnetite formation, which could explain the low iron concentration and increased acidity observed for the first 3 weeks of corrosion. The chromite formation that was observed on 316 SS after 1 week of corrosion is also another likely cause for the initially low iron concentration, as chromite is known to protect steels and enhance corrosion resistance [61,62]. Chromite was observed to form exclusively on 316 SS at the metal-metal contact interface with Zircaloy-4, therefore suggesting that the majority of the chemical interactions seemingly take place at the contact region between 316 SS and Zircaloy-4. The increase in iron concentration after 6 weeks of corrosion could be a result of the eventual dissolution of magnetite as previously shown in Fig. 4c. This can be corroborated with precipitate analysis from the corrosion solution in the 250 °C MilliQ experiments, wherein precipitates were only identifiable after 6 weeks of corrosion either due to no precipitates developing or extremely low quantities forming that prevented XRD identification. The 6-weeklong precipitates were shown to be primarily hematite, which suggests that any magnetite that underwent dissolution was likely oxidized to hematite by residual oxygen in the reaction vessel.

Overall, MilliQ water experiments at 250 °C showed somewhat larger iron oxides with distinct morphologies not observed in the lower temperature experiments. Magnetite was also observed to be a more common iron oxide, and a new secondary phase in the form of chromite was additionally observed. Chromite forms exclusively on 316 SS at the interface that is in contact with Zircaloy-4, further suggesting that most of the chemistry occurring is centralized at the metal-metal interface. It appears that acid-base reactions can influence 316 SS waste canister

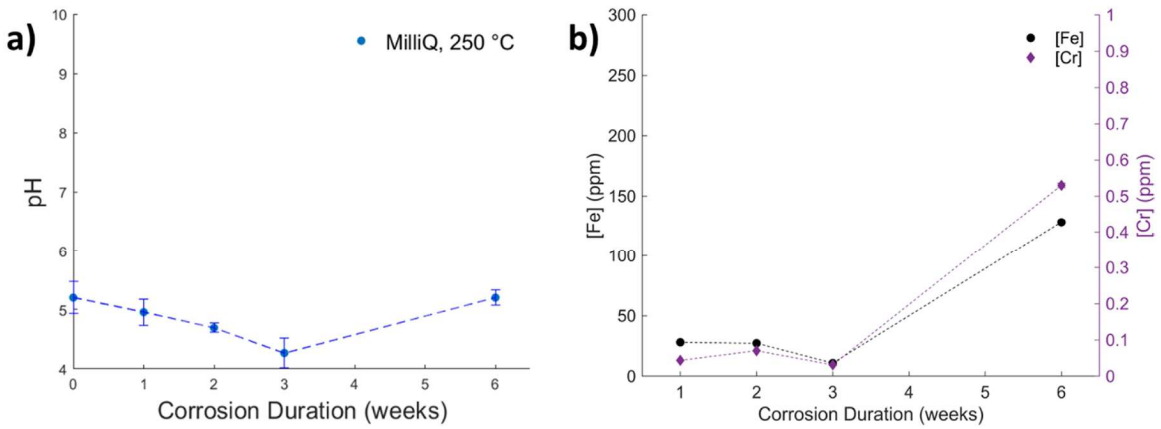


Fig. 5. Aqueous analysis of corrosion experiments at 250 °C in MilliQ water. pH development up to 6 weeks of corrosion a) is shown and b) ICP-MS results of the Fe and Cr concentration as a function of corrosion duration. The error bars in (b) are covered by the data points in the plot. Detection limits for Fe is 0.5 ppb and for Cr is 11 ppt.

behavior due to Eq. (1) being a consistently active reaction throughout MilliQ water experiments regardless of temperature. It can therefore be assumed that upon corrosion of 316 SS, a pH or Fe^{2+} buffer will likely develop to control liquid acidity and iron ion concentration.

3.3. *Corrosion in Mont Terri Water – experiments at 150 °C*

Micrometer-sized iron oxides (1–10 μm) form on the peripheries of both Zircaloy-4 and 316 SS at all interfaces but are more commonly observed at the metal-to-metal interface. Iron oxides adopting an octahedral morphology can be observed beginning 3 weeks into corrosion (Fig. 6a) and could be correlated as magnetite based on previous discussion in the 250 °C MilliQ experiments. As observed during corrosion in MilliQ water, baddeleyite and tetragonal zirconia is identified via GI-XRD as early as 1 week into corrosion (SI Figure S11). Brucite ($Mg(OH)_2$) formation originating from the Mont Terri water composition was observed by SEM as early as 1 week into corrosion at all interfaces; EDS maps confirm brucite formation (Fig. 6c).

The pH of the corrosion solution decreases to 6.8 ± 0.2 after 2 weeks of corrosion. Then, the pH increases to a maximum of 8.6 ± 0.3, before stabilizing at 8.2 ± 0.2 after 6 weeks of corrosion. The initial decrease in pH may be caused by formation of hematite, which was detected by Raman spectroscopy after 1 week of corrosion (SI Figure S13). The early detection of hematite is consistent with observations in MilliQ water experiments, which indicates that a similar corrosion mechanism may be occurring. The formation of hematite may therefore be a possible cause for the MilliQ water experiments being consistently below neutral in pH while also explaining the slight decrease in the pH of Mont Terri water before 3 weeks of corrosion. The proposed reaction for the oxidation of Fe^{2+} to form hematite is thus shown below (Eq. (2)) [63]:

$$4Fe^{2+} + O_2 + 4H_2O \rightarrow 2Fe_2O_3\ (\text{hematite}) + 8H^+ \quad (2)$$

As the residual dissolved oxygen in solution and oxygen in the

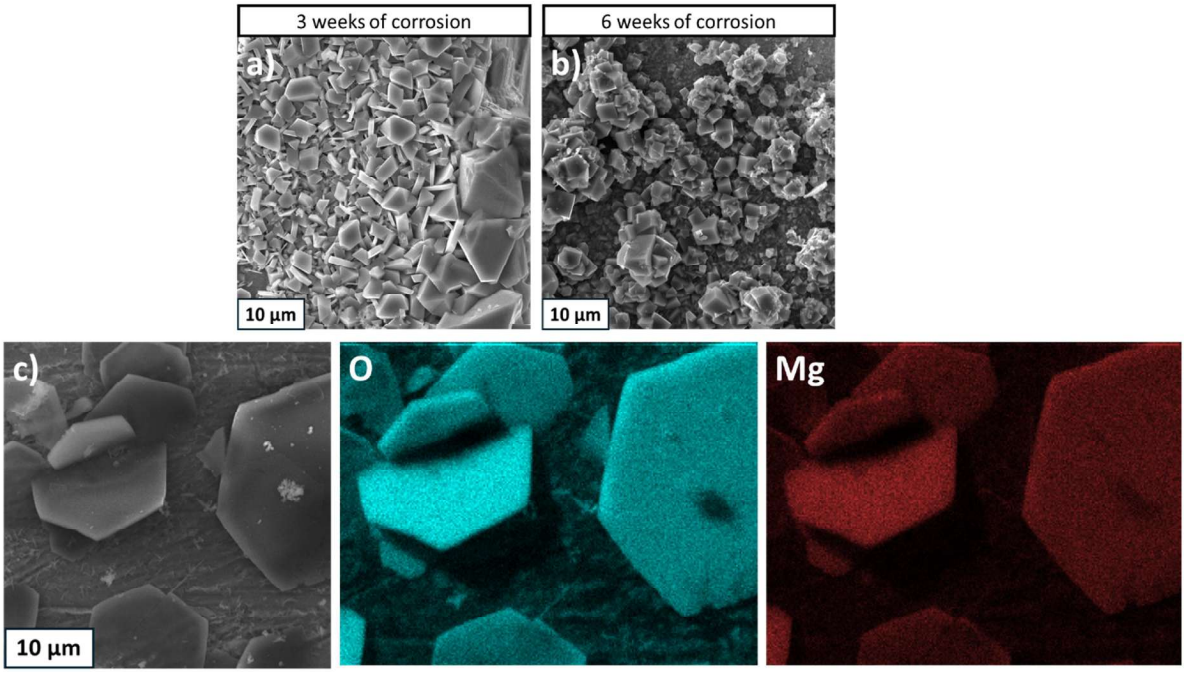


Fig. 6. Solid characterization after corrosion in Mont Terri water at 150 °C. SEM-SE images at the metal-to-metal interface of 316 SS showing iron oxides of different morphologies after a) 3 weeks and b) after 6 weeks of corrosion. c) SEM-SE image and EDS maps showing what is likely brucite formation after 1 week. Full EDS spectrum results are provided in the SI Figure S12.

headspace is depleted, the formation of hematite (Eq. (2)) stops, and the oxidation of Fe^0 to Fe^{2+} likely becomes the dominant reaction for the oxidation of iron (Eq. (3)) [63], leading to the pH increase observed 3 weeks into corrosion.

$$Fe^0 + 2H^+ \rightarrow Fe^{2+} + H_2 \quad (3)$$

The pH increase coincides with the formation of octahedral magnetite. Unlike 150 °C samples corroded for a shorter duration, Raman after 3 weeks of corrosion showed magnetite (SI Figure S13). This observation implies that the increase in pH after three weeks of corrosion signifies a lowering of redox potential such that magnetite forms preferentially over other iron oxides. Compared to the MilliQ water experiments at the same temperature, the preferential formation of magnetite in Mont Terri water suggests that the Mont Terri groundwater will naturally trend towards a more reducing redox potential, thereby hindering the oxidation of iron to fully oxidized hematite.

ICP-MS analysis shows iron to be the most abundant species in solution, followed by Ni, Cr, and Zr (Fig. 7). The Fe concentration steadily increases from ~68 ppm to ~206 ppm with corrosion duration. Again, Fe and Cr show a similar trend. However, in contrast to previous observations in MilliQ, the Zr concentration also shows the same increasing trend with increasing reaction time. Overall, the Zr concentration is 376 % higher in Mont Terri water than in MilliQ water after 6 weeks of corrosion. The Fe concentration reaches ~200 ppm after 6 weeks of corrosion, which is 77.6 % higher than the concentration observed in MilliQ water after the same time and temperature, suggesting an overall more corrosive environment in Mont Terri water. These results alongside pH measurement trends show that redox-based reactions play a larger role on experiments conducted in Mont Terri water, where Eq. (3) appears to dominate in place of Eq. (1) after 3 weeks of corrosion. The rising pH and iron concentration after 3 weeks of corrosion would imply the forward reaction of Eq. (1), which is not in agreement with solid phase analysis revealing magnetite to be the preferred iron oxide. Therefore, it is likely that the ions in the Mont Terri solution are promoting more redox reactions such that the observed pH increase and subsequent magnetite formation are caused by Eq. (3) instead of Eq. (1).

In contrast to the MilliQ water experiments, 150 °C Mont Terri water experiments are able to produce an increase in pH and develop a preference for magnetite formation over hematite, if given enough time. Therefore, while more oxidation does occur, the Mont Terri water will more readily trend to reducing redox potentials even when the initial conditions are slightly oxidizing. This may have implications in a repository scenario where groundwater with non-negligible oxidizing strength manages to interact with the waste canister, as results suggest that the redox conditions may be appreciably lowered by the gradual corrosion of 316 SS. The Mont Terri water could also be able to resist acidification by facilitating Eq. (3) while also buffering the solution through formed brucite.

3.4. Corrosion in Mont Terri water – experiments at 250 °C

Micrometer-sized iron oxides (1–10 μm, occasionally 10 - 15 μm) form on the peripheries of both Zircaloy-4 and 316 SS at the metal-to-metal interface, again with a strong preference to form at the metal-to-metal interface. Tabular and polyhedral morphologies are commonly observed (Fig. 8*a* + *b*). However, the octahedron morphology is more commonly observed in the 250 °C experiments than in 150 °C corrosion experiments in Mont Terri water. Synthesized magnetite commonly adopts an octahedral morphology [50–52] and is once again confirmed by Raman analysis on octahedral crystals viewed on the Raman microscope showing Raman bands strongly representative of magnetite (SI Figure S14). Since increased temperature corrosion experiments were performed to accelerate corrosion and mimic DGR relevant conditions, this suggests that corrosion of the 316 SS canister will lead to preference magnetite formation. HCh thermodynamic modeling discussed in Section 4 verifies that the higher temperature experiments will not cause different oxide phases to form, as magnetite remains the thermodynamically preferred iron oxide at temperatures below 250 °C.

Similarly to MilliQ experiments at 250 °C, nanometer platelets orthogonal to the coupon can be observed only at the metal-to-metal interface of 316 SS (Fig. 8c) and seem to form as early as 1 week into corrosion. EDS analysis showed that the platelets are a chromium-based phase with low iron content (Fig. 8d). GI-XRD analysis at the general location probed by SEM-EDS analysis suggests that the chromium-rich phase is chromite (Fig. 8e). Zircaloy-4 analysis was essentially identical to the 250 °C MilliQ water results, suggesting that the water composition of synthetic Mont Terri water has negligible influence towards Zircaloy-4 corrosion.

Similar to Mont Terri corrosion experiments performed at 150 °C, the pH initially decreases (pH + 5.9 after 2 weeks) before it reaches 8.0 after 6 weeks into corrosion. The pH values of the 250 °C Mont Terri water experiments were consistently observed to be lower than in the 150 °C Mont Terri water experiments but nonetheless reach the same general pH value of 8, showing that corrosion of 316 SS waste canister in contact with Zircaloy-4 cladding will eventually stabilize to slightly alkaline conditions. Although, the increase in pH for Mont Terri water appears to be delayed by at least 1 week at 250 °C (Fig. 9a). Since the decrease in pH coincides with chromite formation, it may be contributing to the lowered pH and delayed rise in pH by hindering Eq. (3), thus making the non-redox reaction of Eq. (1) being more pronounced. ICP-MS results

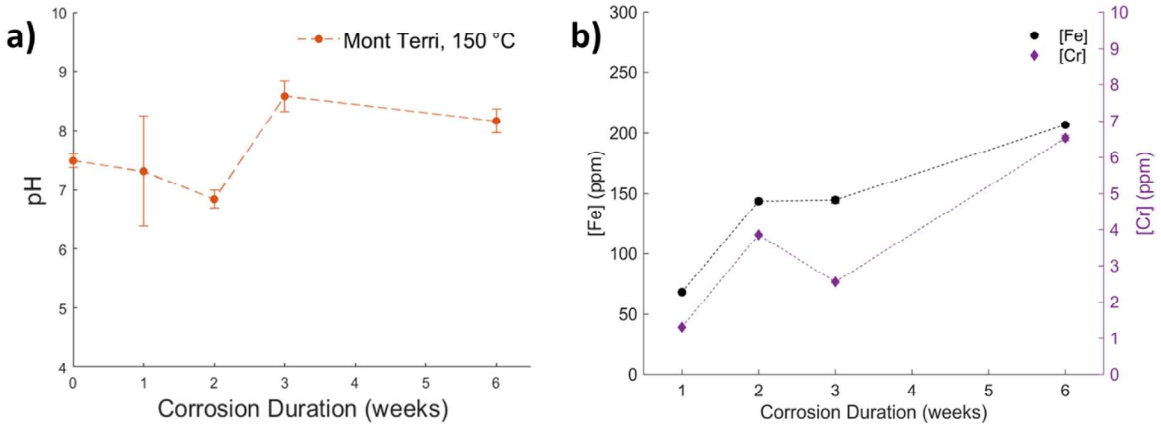


Fig. 7. Aqueous analysis of corrosion experiments at 150 °C in Mont Terri water. a) pH development and b) ICP-MS results of the Fe and Cr concentrations as a function of corrosion duration. The error bars in (b) are covered by the data points in the plot.

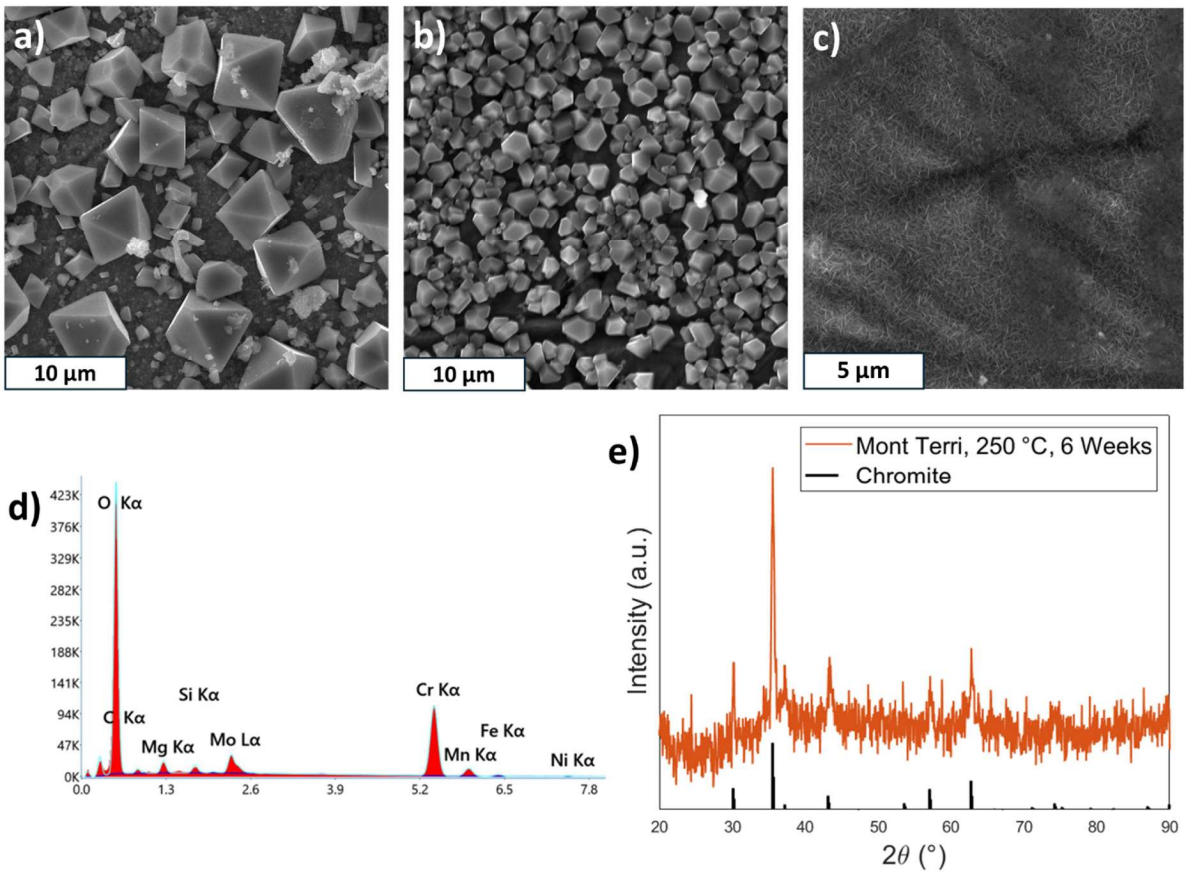


Fig. 8. Solid characterization after corrosion in Mont Terri water at 250 °C. SEM-SE images showing iron oxides of different morphologies at the metal-to-metal interface of 316 SS after 1 week of corrosion. c) SEM-SE image of nanometer sized needle-shaped secondary phases at the metal-to-metal interface of 316 SS with corresponding EDS spectrum showing chromium. e) GI-XRD analysis of area with high Cr-content showing formation of chromite.

may corroborate this phenomenon, which shows low concentrations of chromium in solution and suggests that chromite was formed.

Solution analysis via ICP-MS shows Fe to be the most abundant species in solution, followed by Ni. In contrast to all other experiments, the Cr concentration for corrosion in Mont Terri water at 250 °C is lower (~0.7 ppm after 1 week and ~0.1 ppm after 6 weeks of corrosion) and matches the Zr concentration. The Fe concentration increases from ~111 ppm to ~215 ppm during corrosion up to 6 weeks. In contrast to the other reaction conditions, Cr decreased at 250 °C in Mont Terri water while Fe and Zr increased with reaction time. This decrease in chromium concentration may be due to both the Mont Terri water trending towards more reducing conditions as corrosion proceeds and the precipitation of the chromite phase that was also observed in MilliQ water experiments at 250 °C. The pH increase seen from 3 to 6 weeks of corrosion appears to coincide with an increase in iron concentration. Although, due to chromite formation possibly passivating the 316 SS at the metal-metal interface, it is more likely that the forward reaction of Eq. (1) is the main contributor for the increase in pH and iron ion concentration

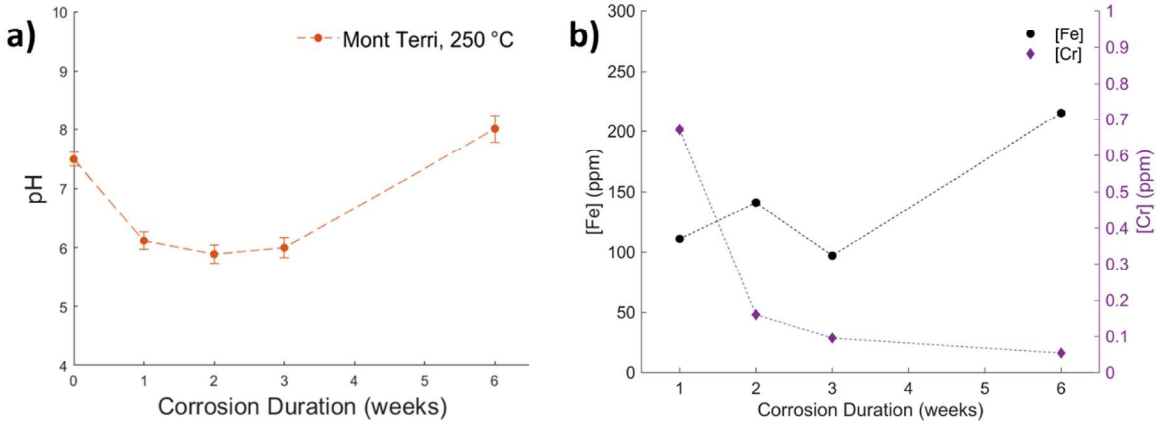


Fig. 9. Aqueous analysis of corrosion experiments at 250 °C in Mont Terri water. (a) pH development up to 6 weeks of corrosion is shown and (b) ICP-MS results of the concentration of iron and chromium as a function of corrosion duration. Error bars in (a) pertain to deviation from calibration curve rather than standard deviation from repeated experiments (SI Equation S1). The error bars in (b) are covered by the data points in the plot.

instead of Eq. (3). Despite the forward reaction of Eq. (1) being proposed, magnetite still appears as a very common phase. A possibility for this explanation is that formed hematite is reduced to magnetite using H_2 as a reducing agent, which has been reported to occur in hydrothermal conditions at temperatures as low as 100 °C [64]. Since redox reactions can be facilitated by the ions transferring charge in Mont Terri water, H_2 is likely already present in the reaction vessel after 6 weeks of corrosion, as oxidation of zirconium into ZrO_2 and the formation of magnetite are able to produce H_2 as a byproduct.

Overall, the Mont Terri water experiments at 250 °C still show signs of being influenced by redox-based reactions due to the large quantities of iron oxides formed and the high iron concentration after a single week of corrosion. Although, chromite formation on the 316 SS surface at the metal-metal interface may hinder iron oxidation which in return may allow for non-redox acid-base reactions to influence the reaction system. Despite the possible passivation by chromite, the accelerated corrosion scenario in Mont Terri water at 250 °C still shows magnetite as the significantly more common iron oxide. Based on these results, magnetite will likely exist as the main iron oxide product instead of hematite over longer time spans in groundwater solutions adjacent to the simulated solution here. If hematite were to form, it would most likely be reduced by H_2 that was produced by oxidation of iron or zirconium.

3.5. *Thermodynamic modeling HCh*

Calculations using the HCh software were performed to predict, pH, speciation of the aqueous solution, and solid phases at thermodynamic equilibrium. Thermodynamic modeling results show that the oxidation of iron strongly influences both the pH and redox potential of the corrosion solution (Fig. 10). Specifically, the oxidation of iron towards thermodynamic equilibrium under probed experimental conditions will lead to an increase in pH and a lowering of the redox potential. The equilibrium speciation of iron in solution shows that iron exists mainly in its +2 oxidation state, with Fe^{2+} and $FeOH^{+}$ being the two most abundant iron species in both MilliQ and Mont Terri water simulations. This implies that the oxidation of iron into Fe^{2+} described in Eq. (3) is the main route for oxidation of iron, as it leads to the pH increase and lowering of redox potential predicted by the model due to the consumption of H^{+} and the formation of H_2, respectively. Although, the pH-increasing effect of iron towards both MilliQ and Mont Terri water diminishes greatly at higher temperatures. This may be due to the autoionization of H_2O being more favored at elevated temperatures up to 250 °C [65]. The addition of the other major elements of 316 SS besides i.e. Cr, Ni, the waste canister material and the cladding material, i.e. Zr into the model showed negligible effects on pH and redox potential in both water compositions within the probed temperature range of 25 – 250 °C (SI Figure S15 and S16). This indicates that the oxidation of iron is the main contributor in controlling the pH and redox potential at thermodynamic equilibrium, which agrees with the consistent observation of iron oxides and high iron concentrations in the experimental results.

HCh predicts all iron, chromium, and zirconium to be oxidized at equilibrium at all probed temperatures and water chemistries. Newly formed phases are predicted to be magnetite, chromite, baddeleyite, and H_2 gas; nickel in the 316 SS remains stable and was not predicted to oxidize or form a secondary phase. These proposed secondary phases are consistent with the secondary phases observed experimentally. This indicates that the hydrothermal corrosion experiments will trend to reducing conditions and an increased pH if corrosion were to proceed past the probed duration of 6 weeks. While H_2 was not measured, the formation of H_2 gas is very likely due to observation of baddeleyite, which requires oxidation of zirconium and produces H_2 as a byproduct [66]. Chromite was also predicted to form at temperatures below 250 °C but was not observed in the hydrothermal corrosion experiments at 150 °C. Because the thermodynamically predicted chromite was only observed to form in experiments at 250 °C specifically on the metal-metal interface with 316 SS in contact with Zircaloy-4 and not at the 316 SS metal-water interface, Zircaloy-4 contact appears to accelerate the corrosion of 316 SS to thermodynamic equilibrium.

This observed effect could be due to galvanic corrosion based on the difference in nobility between 316 SS and zirconium [67]. However, corrosion coupling experiments (Schlain et al. 1955) with zirconium in contact with 316 SS showed no noticeable corrosion effect between the materials [68]. Moreover, galvanic corrosion of zirconium and its alloy is not expected when in contact with steel vessels such as carbon steel according to Shoesmith [8]. Another cause for this observed effect may be due to the confined interface between the 316 SS and Zircaloy-4 generating a chemical environment that is different from the bulk solution. Prior hydrothermal corrosion studies involving 316 SS in contact with clay, glass, and ceramics in simulated DGR environments have reported similar phenomena [14,49,69].

It has been proposed that the accelerated corrosion of 316 SS at an interface with a dissimilar material leads to changes in both solution chemistry and acidity localized at the confined interface, likely caused by the accumulation of metal cations hydrolyzing water [69]. Experimental results appear to agree with the proposed mechanism, as the accumulation of iron cations at the confined interface can explain the observed disparity between iron oxide formation at the metal-metal interface and metal-water interface. Hydrolysis by the iron cations can then lower pH [70], which can assist in explaining the consistent below-neutral pH in the MilliQ water experiments as well as the initial pH decrease observed in the Mont Terri experiments. Prior corrosion coupling studies [68] did not show signs of accelerated corrosion at the metal interface between 316 SS and Zircloy-4 but were conducted at

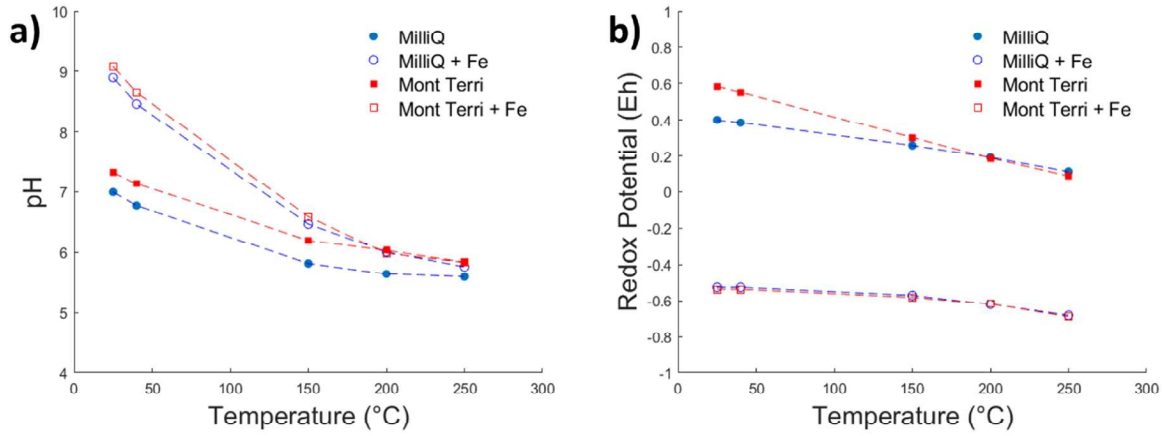


Fig. 10. (a) Computational results of the influence of iron in MilliQ and Mont Terri water towards pH and (b) redox potential at thermodynamic equilibrium.

significantly lower temperatures (35 °C [68]) compared to our accelerated corrosion scenario experiments. Further investigation may need to be done to better determine the cause of seemingly increased corrosion at the interface between 316 SS and Zircaloy-4. Nonetheless, the consistency between the formed secondary phases both computationally and experimentally imply that the hydrothermal corrosion experiments trend towards thermodynamic equilibrium. This consistency additionally suggests that iron corrosion in 316 SS waste canisters will control the pH and redox potential of intruding groundwater in a case of technical barrier failure.

One difference between computational and experimental results is that hematite was observed experimentally but not predicted to form at thermodynamic equilibrium. A possible explanation for this discrepancy is that the oxygen present in the air of the headspace of the reaction vessel leads to more oxidizing conditions to assist in hematite formation. Another possible reason for the discrepancy between modeling and experiment is that the experiments remained very far from thermodynamic equilibrium given that only a small portion of the overall coupon has been corroded. Additionally, the initial conditions of the MilliQ and Mont Terri solutions may be oxidizing enough to have hematite form to then later be reduced into magnetite as the model approaches thermodynamic equilibrium. This may be supported by the computationally reported redox potentials of the two water solutions in the absence of the metals described in Fig. 10b, where both solutions were reported to have a slightly oxidizing potential over 0 V vs. Standard Hydrogen Electrode (SHE) up to a temperature of 250 °C.

The proposed reactions at the 316 SS/Zircaloy interface are shown in Fig. 11. Iron from 316 SS is initially oxidized to Fe^{2+}, producing H_2 which likely caused the pH increase in corrosion experiments with Mont Terri water (Eq. (3)). Experiments conducted with MilliQ water instead show the pH to be slightly acidic, likely caused by preferred hematite formation that may result in the production of H^+ in solution (Eq. (2)). Due to the reduced oxygen solubility in the saline Mont Terri water, magnetite becomes the preferred iron oxide instead of hematite. This transition to preferential magnetite formation will allow for the majority of Fe^{2+} to undergo the Schikorr reaction [71], wherein the protons of water oxidize Fe^{2+} to form the Fe^{2+}/Fe^{3+} oxide [72,73]. During hydrothermal corrosion at 250 °C, chromite forms as a chromium-containing secondary phase exclusively at the metal-metal interface of 316 SS which suggests a possible galvanic corrosion effect involving Zircaloy-4, or the confined interface providing an environment different from the bulk solution to stimulate 316 SS corrosion.

3.6. Solid phase redox pairs

The redox potential between solid phases was determined based on the reported E_{cell} (V) values vs. SHE and the Gibbs free energy relation to evaluate the spontaneity of the redox reactions between solid phases:

$$\Delta G = -nFE_{cell} \tag{4}$$

Results show magnetite to be the preferred phase in the iron/magnetite and magnetite/hematite redox pairs at the experimental temperatures of 150 °C and 250 °C:

$$3Fe + 4H_2O \rightarrow Fe_3O_4 + 4H_2 \quad \begin{matrix} E_{cell}(150^\circ C) = 0.004V \\ E_{cell}(250^\circ C) = 0.028V \end{matrix} \tag{5}$$

$$Fe + Fe_2O_3 + H_2O \rightarrow Fe_3O_4 + H_2 \quad \begin{matrix} E_{cell}(150^\circ C) = 0.095V \\ E_{cell}(250^\circ C) = 0.12V \end{matrix} \tag{6}$$

$$3Fe_2O_3 + H_2 \rightarrow 2Fe_3O_4 + H_2O \quad \begin{matrix} E_{cell}(150^\circ C) = 0.268V \\ E_{cell}(250^\circ C) = 0.271V \end{matrix} \tag{7}$$

The identification of magnetite as early as 1 week into corrosion in both MilliQ and Mont Terri corrosion experiments implies that Eq. (5) is likely an active redox pair as soon as corrosion initiates. However, the preference of magnetite in the magnetite/hematite redox pair appears to be slightly suppressed due to the presence of hematite in 3-week corrosion experiments. This appears to be most pronounced in MilliQ water experiments, where hematite remains commonly observed past 3 weeks of corrosion. This may be due to the formation of magnetite from iron described in Eq. (5) being controlled by other factors in MilliQ water experiments, or by non-redox based interactions between magnetite and hematite. Nonetheless, the repeated identification of magnetite past 1 week across Mont Terri experiments (150 °C and 250 °C) and some MilliQ experiments (250 °C) at the very least implies that the corrosion of the canister/cladding system trends towards low potentials that allow magnetite to be stable. Assuming that corrosion proceeds mainly by Eq. (5), formed hematite may be reduced to magnetite through the use of unoxidized iron (Eq. (6)) or by molecular hydrogen (Eq. (7)). This in return may allow for Fe^{2+} to act as a strong redox buffer in the system, and additionally supports the idea that hematite was not observed at thermodynamic equilibrium due to it being reduced back to magnetite.

The redox potential pair of chromium/chromite was also calculated, showing that chromite formation is spontaneous at 150 °C and 250 °C:

$$Fe^{2+} + 2Cr + 4H_2O \rightarrow FeCr_2O_4 + 3H_2 + 2H^+ \quad \begin{matrix} E_{cell}\ (150^\circ C) = 0.465V \\ E_{cell}(250^\circ C) = 0.503V \end{matrix} \tag{8}$$

Despite chromite formation being predicted by HCh to be spontaneous at 150 °C, no chromite was detected in corrosion experiments conducted at 150 °C which suggests that formation of chromite is slow.

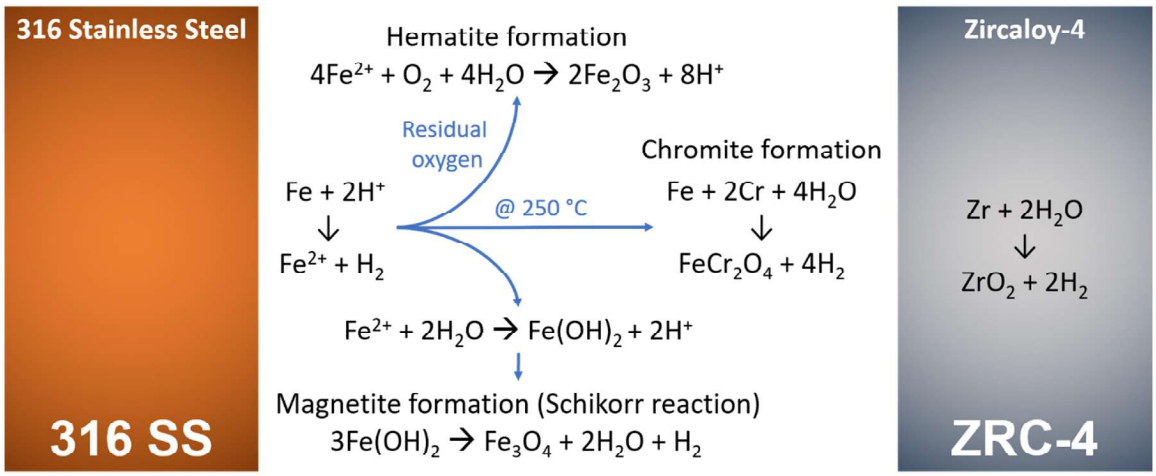


Fig. 11. Proposed reactions at the 316 SS and Zircaloy interface.

The experimental identification of chromite exclusively at the metal-metal interface of 316 SS at 250 °C shows that the contact of Zircaloy-4 on the 316 SS surface may accelerate the corrosion of 316 SS to the thermodynamic equilibrium predicted by the HCh software. While temperature may be playing a role in assisting chromite formation, the observation that chromite forms exclusively at the metal-metal interface on 316 SS strongly suggests that Zircaloy-4 contact is exerting influence on the growth of chromite on 316 SS. This accelerated corrosion may have implications on the role of 316 SS releasing the redox-buffering Fe^{2+} and H_2 into the corrosion system due to the passivating effects of chromium oxides on steel.

3.7. Non-Redox influences

As previously noted in Eq. (1), it is possible for magnetite and hematite to interact with each other through acid-base interactions instead [45-47]. Given that Eq. (1) was reported to be fast even in reducing conditions [45,47], non-redox reactions may have took place in our experiments and could explain the continued presence of hematite after the consumption of the residual oxygen. The effects of the non-redox Eq. (1) are likely most pronounced in the MilliQ water experiments where corrosion is expected to be slower due to the lack of electrolytes facilitating charge transfer for redox reactions. The generally slower corrosion rate by lack of electrolytes and slightly acidic pH measured in MilliQ water experiments may explain why hematite was detected more commonly in MilliQ water experiments; the relatively slow oxidation of iron into magnetite may have been followed by a relatively quick acid-base reaction to leach out Fe^{2+}. This also explains why the characteristic ~667cm^{-1} A_{1g} band of magnetite is often detected as a minor peak along hematite, as not all the Fe^{2+} in magnetite may have been leached out to yet form pure hematite. There is also a possibility that the reverse of Eq. (1) may be occurring in both MilliQ and Mont Terri experiments at 250 °C, which could contribute to the consistently lower pH compared to 150 °C experiments and how magnetite seemingly forms more commonly on the metal coupons.

4. Conclusions

To probe the influences of interfacial contact towards the integrity of the waste canister and cladding material during technical barrier failure, elevated temperature and pressure hydrothermal corrosion experiments were conducted with the waste canister material (316 SS) in contact with the cladding material (Zircaloy-4). Two different water compositions, MilliQ water and Mont Terri water were tested. At 150 °C, formation of hematite, magnetite, and baddeleyite was observed, with chromite additionally forming only at 250 °C on the metal-metal interface. Hematite was detected more commonly on the coupons in MilliQ water, likely due to the lack of electrolytes making magnetite formation slow followed by the relatively fast transformation to hematite. Magnetite, on the other hand, forms preferentially in Mont Terri water after 3 weeks of corrosion which implies a transition to more reducing conditions. Higher temperatures of 250 °C appear to assist in magnetite formation and therefore, assists in achieving more reducing conditions due to the observation of octahedral magnetite in corrosion experiments conducted in both MilliQ and Mont Terri experiments as early as 1 week into corrosion. Chromite was only observed to form at 250 °C at the metal-metal interface, which suggests that the contact of Zircaloy-4 influences the corrosion of 316 SS. Both redox and non-redox reactions involving magnetite and hematite were occurring, with the non-redox reactions taking more influence in the MilliQ water and in scenarios where formed chromite may passivate the 316 SS surface.

Thermodynamic modeling using the HCh software predicts the pH to increase and redox potential to decrease as corrosion proceeds to thermodynamic equilibrium. At equilibrium, magnetite, baddeleyite, and chromite were predicted to form. Thes computational results are consistent with the experimental observations in Mont Terri groundwater and suggests that Mont Terri groundwater will trend to thermodynamic equilibrium. Chromite being a thermodynamically predicted product by HCh, was observed exclusively at the metal-metal interface in our experimental results which suggests that Zircaloy-4 contact influences 316 SS corrosion by seemingly accelerating its corrosion to thermodynamic equilibrium possibly by galvanic corrosion. While the implications for the acceleration of 316 SS corrosion by Zircaloy-4 contact is still unknown, the accelerated corrosion may allow for further release of Fe^{2+} and H_2 into the intruding groundwater to provide a redox buffer when the canister and cladding fail. This may help in ensuring that the redox potential of the intruding water remains reducing throughout the lifespan of the repository even during barrier failure.

Copyright notice

This manuscript has been authored by UT-Battelle, LLC, under contract DE-AC05–00OR22725 with the US Department of Energy (DOE). The US government retains and the publisher, by accepting the article for publication, acknowledges that the US government retains a nonexclusive, paid-up, irrevocable, worldwide license to publish or reproduce the published form of this manuscript, or allow others to do so, for US government purposes. DOE will provide public access to these results of federally sponsored research in accordance with the DOE Public Access Plan (https://www.energy.gov/doe-public-access-plan).

CRediT authorship contribution statement

Steven Nguyen: Writing – review & editing, Writing – original draft, Validation, Investigation, Data curation. **Juliane Weber:** Writing – review & editing, Writing – original draft, Supervision, Funding acquisition, Conceptualization. **Maximilian Zhang:** Writing – review & editing, Visualization, Data curation. **Florie Caporuscio:** Writing – review & editing, Methodology, Funding acquisition, Conceptualization. **Artaches Migdissov:** Writing – review & editing, Supervision, Methodology, Funding acquisition, Conceptualization. **Marlena Rock:** Writing – review & editing. **Sarah Finkeldei:** Writing – review & editing, Writing – original draft, Supervision, Funding acquisition, Conceptualization.

Declaration of competing interest

The authors declare that they have no known competing financial interests or personal relationships that could have appeared to influence the work reported in this paper.

Acknowledgments

The authors would like to acknowledge funding support by the DOE Office of Nuclear Energy's Nuclear Energy University Programs (NEUP, Federal grants DE-NE0009169), and support from the Irvine Materials Research Institute and Laser Spectroscopy Lab at the University of California, Irvine. JW's contribution on manuscript revisions was supported by the U.S. Department of Energy, Office of Science, Office of Basic Energy Sciences, Chemical Sciences, Geosciences, and Biosciences Division.

Supplementary materials

Supplementary material associated with this article can be found, in the online version, at doi:10.1016/j.jnucmat.2026.156516.

Data availability

Data will be made available on request.

References

[1] R.C. Ewing, Long-term storage of spent nuclear fuel, Nat. Mater. 14 (3) (2015) 252–257, https://doi.org/10.1038/nmat4226.

[2] M. Larson, W. Ray, S. Stewart, S. Smith, A. Hackett, N. Burchfield, B. Stinson, Geology and Design of Major Spent Fuel Repositories, Oak Ridge National Laboratory (ORNL), Oak Ridge, TNUnited States, 2020, https://doi.org/10.2172/1731041.

[3] R.B. Rebak, Selection of Corrosion Resistant Materials for Nuclear Waste Repositories, USDOE, Las Vegas, Nevada, 2006, https://doi.org/10.2172/894820.

[4] N. Finck, N. Morelová, M.L. Schlegel, D. Schild, S. Reguer, K. Dardenne, H. Geckeis, Corrosion of Austenitic stainless steel at 90 °c under highly saline and anoxic conditions: a Microspectroscopic study, Corros. Sci. 220 (2023) 111265, https://doi.org/10.1016/j.corsci.2023.111265.

[5] Sakuragi, Tomofumi; Yoshida, Satoshi; Kinugasa, Junichiro; Kato, Osamu; & Tateishi, Tsuyoshi. (2016). Corrosion kinetics of stainless steel by hydrogen measurement under deep geological repository condition - 16047.

[6] S. Necib, M.L. Schlegel, C. Bataillon, S. Daumas, N. Diomidis, P. Keech, D. Crusset, Long-term corrosion behaviour of carbon steel and stainless steel in opalinus clay: influence of stepwise temperature increase, Corros. Eng. Sci. Technol. 54 (6) (2019) 516–528, https://doi.org/10.1080/1478422X.2019.1621456.

[7] E. Hillner, D. Franklin, J. Smee, The Corrosion of Zircaloy-Clad Fuel Assemblies in a Geologic Repository Environment, Bettis Atomic Power Laboratory, West Mifflin, PA, 1998. WAPD-T-3173.

[8] D.W. Shoesmith, D. Zagidulin, The corrosion of zirconium under deep geologic repository conditions, J. Nucl. Mater. 418 (1–3) (2011) 292–306, https://doi.org/10.1016/j.jnucmat.2011.07.028.

[9] A.G. Ilgen, K. Leung, L.J. Criscenti, J.A. Greathouse, Adsorption at nanoconfined solid–water interfaces, Annu. Rev. Phys. Chem. 74 (1) (2023) 169–191, https://doi.org/10.1146/annurev-physchem-083022-030802.

[10] R.K. Kalluri, D. Konatham, A. Striolo, Aqueous NaCl Solutions within charged carbon-slit pores: partition coefficients and density distributions from molecular dynamics simulations, J. Phys. Chem. C 115 (28) (2011) 13786–13795, https://doi.org/10.1021/jp203086x.

[11] F.C. Meldrum, C. O'Shaughnessy, Crystallization in Confinement, Adv. Mater. 32 (31) (2020), https://doi.org/10.1002/adma.202001068.

[12] S. Senapati, A. Chandra, Dielectric constant of water confined in a nanocavity, J. *Phys. Chem. B* 105 (22) (2001) 5106–5109, https://doi.org/10.1021/jp011058i.

[13] J. Martí, G. Nagy, E. Guàrdia, M.C. Gordillo, Molecular dynamics simulation of liquid water confined inside graphite channels: dielectric and dynamical properties, J. Phys. Chem. B 110 (47) (2006) 23987–23994, https://doi.org/10.1021/jp0647277.

[14] M.C. Cheshire, F.A. Caporuscio, C.F. Jové Colón, K.E. Norskog, Fe-saponite growth on low-carbon and stainless steel in hydrothermal-bentonite experiments, J. Nucl. Mater. 511 (2018) 353–366, https://doi.org/10.1016/j.jnucmat.2018.09.038.

[15] F.A. Caporuscio, K.B. Sauer, M.J. Rock, Argillite Disposal R&D – LANL (FY19), 2019. Los AlamosReport LA-UR-19-24397.

[16] F.J. Pearson, Schweiz (Eds.), Mont Terri Project - Geochemistry of Water in the Opalinus Clay Formation at the Mont Terri Rock Laboratory, Berichte des BWG Serie Geologie; BWG, Bern, 2003.

[17] E.C. Gaucher, P. Blanc, Cement/Clay Interactions – A review: experiments, natural analogues, and modeling, Waste Manag. 26 (7) (2006) 776–788, https://doi.org/10.1016/j.wasman.2006.01.027.

[18] Y. Barakat, Y.-J. Cui, N. Mokni, P. Delage, F. Bernier, Impact of alkalinity on the swelling behavior of opalinus clay, E3S Web. Conf. 205 (2020) 13017, https://doi.org/10.1051/e3sconf/202020513017.

[19] Parr Instrument Company. *Model 4744 General Purpose Acid Digestion Vessel, 45 mL*. https://www.parrinst.com/products/sample-preparation/acid-digestion/general-purpose-acid-digestion-vessel-model-4744-45-ml/ (Accessed December 5, 2025 11:29AM).

[20] Yu.V.HCh Shvarov, New potentialities for the thermodynamic simulation of geochemical systems offered by windows, Geochem. Int. 46 (8) (2008) 834–839, https://doi.org/10.1134/S0016702908080089.

[21] T.J.B. Holland, R. Powell, An internally consistent thermodynamic data set for phases of petrological interest, J. Metamorph. Geol. 16 (3) (1998) 309–343, https://doi.org/10.1111/j.1525-1314.1998.00140.x.

[22] R.E. Stoffregen, C.N. Alpers, J.L. Jambor, Alunite-jarosite crystallography, thermodynamics, and geochronology, Rev. Mineral. Geochem. 40 (1) (2000) 453–479, https://doi.org/10.2138/rmg.2000.40.9.

[23] R.A. Robie, B.S. Hemingway, Thermodynamic Properties of Minerals and Related Substances at 298.15 K and 1 Bar Pressure and at Higher Temperatures, U.S. Geol. Survey, Washington DC, 1995, p. 2131, https://doi.org/10.3133/b2131. Bulletin.

[24] G.B. Naumov, B.N. Ryzhenko, I.L. Khodakovsky, Handbook of Thermodynamic Data (PB-226722/7GA), NTIS, Springfield, Va, 1974, p. 373.

[25] IVTANTERMO, Tables of thermodynamic properties of individual materials on magnetic tape. Data Bank), Mosc.: Inst. Vysok. Temp. Akad. Nauk. SSSR (1983).

[26] Glushko, V.P. and Gurvich, L.V. Thermodynamic properties of individual substances: Volume 1, parts 1 and 2., Dec. 1987.

[27] R.J. Lemire, U. Berner, C. Musikas, D.A. Palmer, P. Taylor, O. Tochiyama, Chemical Thermodynamics of iron. Part 1, Nuclear Energy Agency Data Bank, Organisation for Economic Co-Operation and Development, Ed., vol. 13a, Chemical Thermodynamics, OECD Publications, 2013.

[28] J.W. Johnson, E.H. Oelkers, H.C. Helgeson, SUPCRT92: a software package for calculating the standard molal thermodynamic properties of minerals, gases, aqueous species, and reactions from 1 to 5000 bar and 0 to 1000 °C, Comput. Geosci. 18 (7) (1992) 899–947, https://doi.org/10.1016/0098-3004(92)90029-Q.

[29] E.L. Shock, D.C. Sassani, M. Willis, D.A. Sverjensky, Inorganic species in geologic fluids: correlations among standard molal thermodynamic properties of aqueous ions and hydroxide complexes, Geochim. Cosmochim. Acta 61 (5) (1997) 907–950, https://doi.org/10.1016/S0016-7037(96)00339-0.

[30] D.A. Sverjensky, E.L. Shock, H.C. Helgeson, Prediction of the thermodynamic properties of aqueous metal complexes to 1000 °C and 5 Kb, Geochim. Cosmochim. Acta 61 (7) (1997) 1359–1412, https://doi.org/10.1016/S0016-7037(97)00009-4.

[31] B.R. Tagirov, A.V. Zotov, N.N. Akinfiev, Experimental Study of dissociation of HCl from 350 to 500 °C and from 500 to 2500 bars: thermodynamic properties of HCl° (Aq), Geochim. Cosmochim. Acta 61 (20) (1997) 4267–4280, https://doi.org/10.1016/S0016-7037(97)00274-3.

[32] I.I. Diakonov, J. Schott, F. Martin, J.-C. Harrichourry, J. Escalier, Iron(III) Solubility and Speciation in Aqueous Solutions. Experimental Study and Modelling: part 1. Hematite Solubility from 60 to 300 °C in NaOH–NaCl Solutions and Thermodynamic Properties of $Fe(OH)_4^-$(Aq), Geochim. Cosmochim. Acta 63 (15) (1999) 2247–2261, https://doi.org/10.1016/S0016-7037(99)00070-8.

[33] Mahoney, J.; Strachan, D. *Reduction of Sulfate by Hydrogen in Natural Systems: a Literature Review: salt Repository Project*; PNL/SRP-6667, 7087752, ON: DE89000261; 1988; p PNL/SRP-6667, 7087752, ON: DE89000261. https://doi.org/10.2172/7087752.

[34] P. Wersin, M. Mazurek, T. Gimmi, Porewater chemistry of opalinus clay revisited: findings from 25 years of data collection at the mont terri rock laboratory, Appl. Geochem. 138 (2022) 105234, https://doi.org/10.1016/j.apgeochem.2022.105234.

[35] Yang, G. (2017). Investigations of the Tube Support Plate (TSP) clogging phenomenon in PWR steam generators - understanding and prioritization of its formation mechanisms.

[36] O.N. Shebanova, P. Lazor, Raman spectroscopic study of magnetite ($FeFe_2O_4$): a new assignment for the vibrational spectrum, J. Solid. State Chem. 174 (2) (2003) 424–430, https://doi.org/10.1016/S0022-4596(03)00294-9.

[37] D.L.A. De Faria, S. Venâncio Silva, M.T. De Oliveira, Raman microspectroscopy of some iron oxides and oxyhydroxides, J. Raman Spectrosc. 28 (11) (1997) 873–878, https://doi.org/10.1002/(SICI)1097-4555(199711)28:11≤873::AID-JRS177≥3.0.CO;2-B.

[38] M. Legodi, D. Dewaal, The preparation of magnetite, goethite, hematite and maghemite of pigment quality from mill scale iron waste, Dyes Pigments 74 (1) (2007) 161–168, https://doi.org/10.1016/j.dyepig.2006.01.038.

[39] F.J. Owens, J. Orosz, Effect of nanosizing on lattice and magnon modes of hematite, Solid State Commun. 138 (2) (2006) 95–98, https://doi.org/10.1016/j.ssc.2006.01.049.

[40] M.J. Massey, U. Baier, R. Merlin, W.H. Weber, Effects of pressure and isotopic substitution on the raman spectrum of α-fe_2o_3: identification of two-magnon scattering, Phys. Rev. B 41 (11) (1990) 7822–7827, https://doi.org/10.1103/PhysRevB.41.7822.

[41] S. Yin, R. Wirth, H. He, C. Ma, J. Pan, J. Xing, J. Xu, J. Fu, X.-N. Zhang, Replacement of magnetite by hematite in hydrothermal systems: a refined redox-independent model, Earth Planet. Sci. Lett. 577 (2022) 117282, https://doi.org/10.1016/j.epsl.2021.117282.

[42] B.L. Davis, G. Rapp, M.J. Walawender, Fabric and structural characteristics of the martitization process, Am. J. Sci. 266 (6) (1968) 482–496, https://doi.org/10.2475/ajs.266.6.482.

[43] L.B. Salviano, T.M.D.S. Cardoso, G.C. Silva, M.S.S. Dantas, A.D.M. Ferreira, Microstructural Assessment of Magnetite Nanoparticles (Fe3O4) Obtained by Chemical Precipitation Under Different Synthesis Conditions, Mat. Res. 21 (2) (2018), https://doi.org/10.1590/1980-5373-mr-2017-0764.

[44] I.V. Chernyshova, M.F. Hochella Jr, A.S. Madden, Size-dependent structural transformations of hematite nanoparticles. 1. Phase Transition, Phys. Chem. Chem. Phys. 9 (14) (2007) 1736, https://doi.org/10.1039/b618790k.

[45] T. Otake, D.J. Wesolowski, L.M. Anovitz, L.F. Allard, H. Ohmoto, Experimental evidence for non-redox transformations between magnetite and hematite under h2-rich hydrothermal conditions, Earth Planet. Sci. Lett. 257 (1–2) (2007) 60–70, https://doi.org/10.1016/j.epsl.2007.02.022.

[46] H. Ohmoto, Nonredox transformations of magnetite-hematite in hydrothermal systems, Econ. Geol. 98 (1) (2003) 157–161, https://doi.org/10.2113/gsecongeo.98.1.157.

[47] T. Otake, D.J. Wesolowski, L.M. Anovitz, L.F. Allard, H. Ohmoto, Mechanisms of iron oxide transformations in hydrothermal systems, Geochim. Cosmochim. Acta 74 (21) (2010) 6141–6156, https://doi.org/10.1016/j.gca.2010.07.024.

[48] J.L. Bañuelos, E. Borguet, G.E. Brown Jr, R.T. Cygan, J.J. DeYoreo, P.M. Dove, M. P. Gaigeot, F.M. Geiger, J.M. Gibbs, V.H. Grassian, A.G. Ilgen, Oxide–and silicate–water interfaces and their roles in technology and the environment, Chem. Rev. 123 (10) (2023) 6413–6544.

[49] M.C. Cheshire, F.A. Caporuscio, M.S. Rearick, C. Jove-Colon, M.K. McCarney, Bentonite evolution at elevated pressures and temperatures: an experimental study for generic nuclear repository designs, Am. Mineral. 99 (8–9) (2014) 1662–1675, https://doi.org/10.2138/am.2014.4673.

[50] H. Qi, J. Ye, N. Tao, M. Wen, Q. Chen, Synthesis of Octahedral magnetite microcrystals with high crystallinity and low coercive field, J. Cryst. Growth 311 (2) (2009) 394–398, https://doi.org/10.1016/j.jcrysgro.2008.10.110.

[51] J.M. Bigham, R.W. Fitzpatrick, D.G. Schulze, Iron Oxides, in: J.B. Dixon, D. G. Schulze (Eds.), *SSSA Book Series* 7, Wiley, 2002, pp. 323–366. https://doi.org/10.2136/sssabookser7.c10.

[52] W. Lei, Y. Liu, X. Si, J. Xu, W. Du, J. Yang, T. Zhou, J. Lin, Synthesis and magnetic properties of octahedral Fe_3O_4 via a one-pot hydrothermal route, Phys. Lett. A 381 (4) (2017) 314–318, https://doi.org/10.1016/j.physleta.2016.09.018.

[53] G. Brunner, Corrosion in Hydrothermal and Supercritical Water, in: Supercritical Fluid Science and Technology, 5, Elsevier, 2014, pp. 591–619, https://doi.org/10.1016/B978-0-444-59413-6.00012-1.
[54] J. Desarnaud, H. Derluyn, J. Carmeliet, D. Bonn, N. Shahidzadeh, Hopper Growth of Salt Crystals, J. Phys. Chem. Lett. 9 (11) (2018) 2961–2966, https://doi.org/10.1021/acs.jpclett.8b01082.
[55] S. Rani, M. Aggarwal, M. Kumar, S. Sharma, D. Kumar, Removal of methylene blue and rhodamine B from water by zirconium oxide/graphene, Water Sci. 30 (1) (2016) 51–60, https://doi.org/10.1016/j.wsj.2016.04.001.
[56] R. Kusaka, Y. Kumagai, M. Watanabe, T. Sasaki, D. Akiyama, N. Sato, A. Kirishima, Raman identification and characterization of chemical components included in simulated nuclear fuel debris synthesized from uranium, stainless steel, and zirconium, J. Nucl. Sci. Technol. 60 (5) (2023) 603–613, https://doi.org/10.1080/00223131.2022.2128460.
[57] Z.W. Zhang, F.X. Gan, Analysis of the chromite inclusions found in nephrite minerals obtained from different deposits using SEM-EDS and LRS, J. Raman Spectrosc. 42 (9) (2011) 1808–1811, https://doi.org/10.1002/jrs.2963.
[58] V. Lughi, D. Lenaz, A. Bonifacio, F. Princivalle, V. Sergo, F.A Raman Parisi, Spectroscopy study of the oxidation processes in synthetic chromite $FeCr_2O4$, Ceram. Int. 46 (18) (2020) 29382–29387, https://doi.org/10.1016/j.ceramint.2020.07.059.
[59] Z.V. Marinković Stanojević, N. Romčević, B. Stojanović, Spectroscopic study of spinel $ZnCr_2O_4$ Obtained from mechanically activated $ZnO–Cr_2O_3$ mixtures, J. Eur. Ceram. Soc. 27 (2–3) (2007) 903–907, https://doi.org/10.1016/j.jeurceramsoc.2006.04.057.
[60] B.J. Reddy, R.L. Frost, Spectroscopic characterization of chromite from the moabaracoa ophiolitic massif, Cuba, Spectrochim. Acta A: Mol. Biomol. Spectrosc. 61 (8) (2005) 1721–1728, https://doi.org/10.1016/j.saa.2004.07.002.
[61] R. Felix-Contreras, La De, J. Vega Olivas, C.D. Arrieta-Gonzalez, J.G. Chacon-Nava, R.A. Rodriguez-Diaz, J.G. Gonzalez-Rodriguez, J. Porcayo-Calderon, Kinetic and thermodynamic aspects of the degradation of ferritic steels immersed in solar salt, Materials 17 (23) (2024) 5776, https://doi.org/10.3390/ma17235776.
[62] Q. Liu, C. Wang, J. Qian, F. Pessu, Investigation of the early stage corrosion characteristics of molten (nitrate) salt – oxide – metal interfaces, and the links to interfacial thermo-mechanical stress, Corros. Sci. 220 (2023) 111282, https://doi.org/10.1016/j.corsci.2023.111282.
[63] M. Pourbaix, Atlas of Electrochemical Equilibria in Aqueous solutions, Pergamon Press, New York, 1966.
[64] K. Yanagisawa, N. Yamasaki, Reduction of haematite to magnetite under controlled hydrothermal conditions with hydrogen gas, J. Mater. Sci. 26 (2) (1991) 473–478, https://doi.org/10.1007/BF00576545.
[65] A.V. Bandura, S.N. Lvov, The ionization constant of water over wide ranges of temperature and density, J. Phys. Chem. Ref. Data 35 (1) (2006) 15–30, https://doi.org/10.1063/1.1928231.
[66] D.W. Shoesmith, D. Zagidulin, The corrosion of zirconium under deep geologic repository conditions, J. Nucl. Mater. 418 (1–3) (2011) 292–306, https://doi.org/10.1016/j.jnucmat.2011.07.028.
[67] Acid, H. Corrosion Resistance of Zircadyne Alloys In Specific Media Hydrochloric Acid; 1998.
[68] D. Schlain, C.B. Kenahan, D.V. Steele, Galvanic corrosion behavior of titanium and zirconium in sulfuric acid solutions, J. Electrochem. Soc. 102 (3) (1955) 102, https://doi.org/10.1149/1.2430003.
[69] X. Guo, S. Gin, P. Lei, T. Yao, H. Liu, D.K. Schreiber, D. Ngo, G. Viswanathan, T. Li, S.H. Kim, J.D. Vienna, J.V. Ryan, J. Du, J. Lian, G.S. Frankel, Self-Accelerated corrosion of nuclear waste forms at material interfaces, Nat. Mater. 19 (3) (2020) 310–316, https://doi.org/10.1038/s41563-019-0579-x.
[70] J.W. Oldfield, W.H. Sutton, Crevice corrosion of stainless steels: I. a mathematical model, Br. Corros. J. 13 (1) (1978) 13–22, https://doi.org/10.1179/000705978798358671.
[71] G. Schikorr, Über Die Reaktionen Zwischen Eisen, seinen Hydroxyden und wasser, Z. Elektrochem. Angew. Phys. Chem. 35 (2) (1929) 65–70, https://doi.org/10.1002/BBPC.19290350204.
[72] M. Booy, T.W. Swaddle, Hydrothermal preparation of magnetite from iron chelates, Can. J. Chem. 56 (3) (1978) 402–403, https://doi.org/10.1139/v78-064.
[73] R.O. Rihan, S. Nešić, Erosion–corrosion of mild steel in hot caustic. Part I: NAOH solution, Corros. Sci. 48 (9) (2006) 2633–2659, https://doi.org/10.1016/j.corsci.2005.09.018.